# Adaptive frequency-domain sliding block correlators for PMCW radar processing

Wu, H.; Leus, G.; Pandharipande, A.

**DOI**
10.1109/JSEN.2025.3633803



**Publication date**
2025

**Document Version**
Final published version

**Published in**
IEEE Sensors Journal

# Adaptive Frequency-Domain Sliding Block Correlators for PMCW Radar Processing

Hanqing Wu, Geert Leus, *Fellow, IEEE*, and Ashish Pandharipande, *Senior Member, IEEE*

***Abstract*—Phase-modulated continuous-wave (PMCW) radars offer better multiple antenna support and flexible waveform design. These radars, however, suffer from the high computational complexity of correlation processing used to obtain the range of targets, particularly due to the use of long code sequences. To address this, we exploit signal sparsity and propose an adaptive sliding block-based fast Fourier transform (FFT) correlator that selectively processes only the relevant range bins and dynamically aligns processing blocks using a time-shift parameter. This sliding mechanism minimizes boundary effects and reduces the number of blocks required for processing. The framework also incorporates external sensor data for context-aware range-bin selection and includes an analytical formulation for optimal block size selection. Simulations demonstrate that the proposed method preserves the signal-to-noise ratio (SNR) and target peaks while significantly reducing processing time. The effectiveness of the proposed method is demonstrated through numerical simulations.**

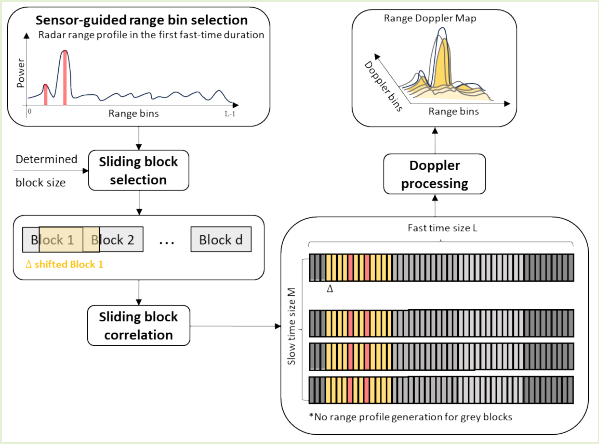


***Index Terms*—Automotive driving, correlator, phase-modulated continuous-wave (PMCW) radar, sliding block fast Fourier transform (FFT).**

## I. Introduction

RADAR is a core sensor technology in automotive driving systems to achieve higher levels of autonomy in a cost-efficient and robust manner. Automotive radar sensors are used to estimate attributes like range, Doppler, and angle of targets in the driving scene [1], [2]. To support higher levels of driving autonomy, finer angular resolution is required with imaging radars that have a large number of antennas [3], [4]. Conventional automotive radars use frequency-modulated continuous-wave (FMCW) signals as active sensor signals. While FMCW radars are attractive for their architectural simplicity, they do not provide sufficient multiple antenna scaling for imaging radar applications and instead lead to a reduced unambiguous Doppler velocity. This has led to interest in phase-modulated continuous-wave (PMCW) digital radars due to inherent support for a large number of antennas [5], [6], [7]. Besides providing a pathway to high-resolution imaging radars, some of the other benefits reported for PMCW radars are waveform design flexibility and reduced inter-radar interference [8], [9], [10], [11].

A PMCW radar uses carefully designed sequences with good correlation properties to achieve multiple-input–multiple-output (MIMO) scaling with high unambiguous Doppler velocity. A simplified block diagram of a binary PMCW radar is shown in Fig. 1. In binary PMCW radars, the transmitted signal is a continuous radio frequency (RF) carrier modulated by a binary sequence, where each symbol, drawn from the set $\{-1, +1\}$, represents a 0° or 180° phase shift. To ensure high performance, binary sequences with good periodic autocorrelation and cross correlation properties [12], [13], such as almost-perfect autocorrelation sequence [14], zero correlation zone [15], and Gold [16] sequences are used to modulate a 79-GHz local oscillator (LO). The modulated signal is then amplified and transmitted as electromagnetic waves by the antennas and reflected back by the targets. The received RF signal is an amplitude-scaled and time-delayed version of the transmitted one with the delays corresponding to the time of flight. It is amplified by a low-noise amplifier (LNA), and after that, the RF signal is downconverted by the

Received 19 September 2025; revised 4 November 2025; accepted 13 November 2025. Date of publication 24 November 2025; date of current version 30 December 2025. This work was supported in part by the Dutch Ministry of Economic Affairs and Climate Policy and in part by the Important Projects of Common European Interest (IPCEI) Microelectronics and Communication Technology (ME/CT) Project. The associate editor coordinating the review of this article and approving it for publication was Dr. Shisheng Guo. *(Corresponding author: Ashish Pandharipande.)*

Hanqing Wu and Ashish Pandharipande are with NXP Semiconductors, 5656 AG Eindhoven, The Netherlands (e-mail: ashish.pandharipande@nxp.com).

Geert Leus is with the Faculty of Electrical Engineering, Mathematics and Computer Science, Delft University of Technology (TU Delft), 2628 CD Delft, The Netherlands.

Digital Object Identifier 10.1109/JSEN.2025.3633803

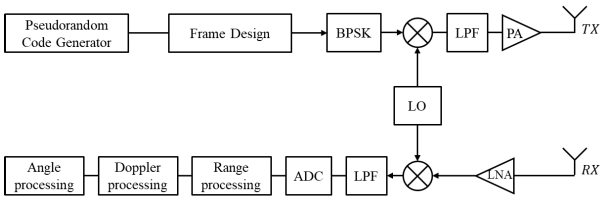


Fig. 1. System model of PMCW radar.

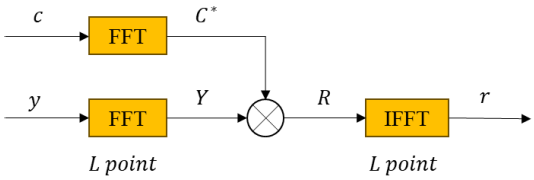


Fig. 2. Block diagram of a frequency-domain correlator.

same LO. After digitization by the analog-to-digital converter (ADC), range, Doppler, and angle processing are done by order to get the position, velocity, and angle information of targets.

Range processing in PMCW radars is conventionally performed using a correlator bank, which estimates the delay of signals reflected from targets. The complexity of correlation processing is quite high due to the large-length PMCW radar sequences used (in the order of thousands). Correlators can be implemented in either the time domain [17], [18], [19], [20] or frequency domain [21], [22]. Time-domain correlators are advantageous for hardware implementations due to their simplicity and parallel processing capabilities, but they are computationally expensive and resource-intensive. In contrast, frequency-domain correlators leverage the efficiency of the fast Fourier transform (FFT) to enable parallel processing across multiple correlation phases, significantly improving computational efficiency.

Besides radar applications, the challenge of designing low-complexity correlators is encountered in other applications like spread-spectrum communications and global navigation satellite system (GNSS) signal acquisition. To decrease the complexity, several fast time-domain algorithms have been proposed [18], [19], [20], and in certain cases, these methods are competitive with FFT-based approaches for large-scale correlations. For frequency-domain correlators, algorithms that exploit FFT splitting have been developed [21], [22], primarily for GNSS signals. However, radar signals exhibit sparsity properties that have yet to be fully explored, presenting an opportunity to develop new methods that reduce computational complexity for radar applications.

We propose an adaptive frequency-domain sliding block correlator for PMCW automotive radar processing. By dynamically selecting and processing only the relevant blocks, the method significantly reduces computational cost for both range and Doppler processing. Unlike our previously proposed fixed-block method [23], the present framework introduces a time-shift parameter that aligns processing blocks with target positions with more flexibility, mitigating boundary effects and enabling more efficient block utilization. We further derive a closed-form design rule for selecting the optimal block number that minimizes the total range and Doppler processing complexity for a given radar configuration, eliminating the need for frame-by-frame tuning. The framework is also flexible. It operates independently based on the initial range profile and can optionally incorporate external scene information (e.g., digital maps), when available, to guide block selection. Simulation results across three exemplary automotive driving scenarios validate the effectiveness of the proposed sliding mechanism, demonstrating reduced redundant processing, improved handling of boundary effects, and robustness in dense, multitarget environments. In all cases, the sliding approach preserves target peaks and the noise floor while achieving substantial runtime reductions compared to full-FFT and nonsliding block correlators [23]. Collectively, these contributions yield a more efficient and robust solution for PMCW automotive radar data processing.

## II. Frequency-Domain Correlator

In a PMCW radar system with a code $c[n]$ of length $L_c$ and symbol duration $T_c$, range processing is performed using a bank of correlators that compare the received signal $y[n]$ with delayed versions of $c[n]$ at $\tau T_c$. The resulting range profile exhibits peaks at time-of-flight reflections, enabling distance estimation. Since time-domain correlation corresponds to element-wise multiplication in the frequency domain, the range profile $r[\tau]$ can be computed using the FFT, element-wise multiplication, and inverse FFT, as shown in Fig. 2. For efficient FFT implementation, signals are zero-padded to a power-of-two length $L$.

The FFT-transformed received and transmitted signals are, respectively,

$$Y[k] = \sum_{n=0}^{L-1} y[n]\, e^{-j\frac{2\pi}{L}kn}, \quad C[k] = \sum_{n=0}^{L-1} c[n]\, e^{-j\frac{2\pi}{L}kn}. \tag{1}$$

The frequency-domain correlation is then obtained as

$$\begin{aligned} R[k] &= Y[k]\, C^*[k] \\ &= \sum_{\tau=0}^{L-1} \underbrace{\sum_{n=0}^{L-1} y[n]\, c[(n-\tau) \bmod L]}_{r[\tau]}\, e^{-j\frac{2\pi}{L}k\tau}. \end{aligned} \tag{2}$$

A subsequent IFFT results in the time-domain range profile

$$r[\tau] = \frac{1}{L} \sum_{k=0}^{L-1} R[k]\, e^{j\frac{2\pi}{L}k\tau}. \tag{3}$$

Although this frequency-domain approach has a reduced complexity of $\mathcal{O}(L \log L)$ compared to time-domain correlators, it remains computationally demanding for large $L_c$, motivating the need for lower complexity approaches.

## III. Adaptive FFT-Based Sliding Block Correlator

In automotive radar scenarios, only a limited number of targets exist within the radar's field of view. Consequently, radar signals exhibit inherent sparsity, with many range bins

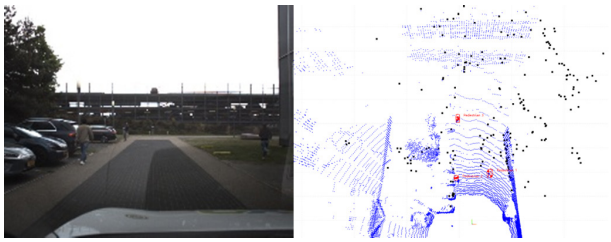

Fig. 3. Illustration showing sparsity in range domain using a conventional FMCW radar. Black points: radar detections, blue points: LiDAR detections, and red boxes: bounding boxes on detected targets.

containing minimal or no relevant target information, and only a small subset of detections being relevant. Furthermore, in advanced driver-assistance system applications, the nearby targets are more relevant for actions like braking and cruise control. As such, the detection of only the close-by targets is relevant. An exemplary real-world radar and LiDAR measurement data is shown in Fig. 3. Here, three targets are detected within 15 m, while detections beyond this range contain no meaningful target information, illustrating the sparse nature of radar returns. Note that this example uses a conventional radar (not PMCW) and is included to illustrate the general sparsity observed in automotive radar scenes.

Leveraging range sparsity, we propose an adaptive FFT-based sliding block correlator that reduces computational complexity compared to conventional full-length frequency-domain processing. Instead of performing correlation across the entire range profile, the proposed method partitions the full-length correlation into $d$ smaller blocks, dynamically identifies and processes only the relevant range profile blocks where potential targets are likely to be present. Unlike fixed-block partitioning [23], which may require redundant block processing or risk target misalignment near block boundaries, we introduce a sliding block mechanism controlled by a tunable time-shift parameter $\Delta$. This mechanism ensures that targets are well-contained within their corresponding blocks with sufficient margins, thereby enhancing robustness and reducing computational complexity.

While primarily designed for range processing, the proposed method operates within a broader radar framework that includes Doppler processing, as illustrated in Fig. 4. In the first fast-time duration, a full-range profile is computed to determine the block indices and the corresponding time shift $\Delta$ associated with potential targets. For the remaining $M-1$ fast-time durations, the adaptive sliding block correlator is applied to obtain only these selected range blocks. Finally, Doppler processing is performed exclusively on the adaptively selected blocks across all $M$ pulses, thereby further reducing the computational load by avoiding full range–Doppler processing.

Building on this principle, we next detail how the adaptive sliding block correlator is formulated and applied. We first provide a mathematical explanation of how segmentation into $d$ blocks and the application of a time shift $\Delta$ allows direct computation of the correlation values for a selected sliding block, ensuring equivalence to the full-length frequency-domain correlator. Based on this formulation, we then describe the processing framework step by step, including the identification of relevant range bins, determination of the optimal time shift, and frame-to-frame adaptation.

### A. Adaptive Sliding Block Correlator

This section provides a mathematical description of the adaptive sliding block correlator. As illustrated in Fig. 5, we show how segmentation of the received and reference signals, combined with phase compensation, enables direct computation of the correlation values for the desired sliding block, providing the corresponding portion of the full correlation output without computing the entire range profile.

*1) Padding and Segmentation:* The received $y[n]$ is first zero-padded to a length $L$ that is a multiple of $d$ and a power of 2 and then segmented into $d$ blocks $y_i[n]$, $i = 1, 2, \ldots, d$, where

$$y_i[n] = y\left[n + (i-1)\,L/d\right], \quad n \in \{0, 1, \ldots, L/d - 1\}. \tag{4}$$

Note that the transmitted code sequence $c[n]$ is processed similarly and could be precomputed for storage.

*2) Combination:* In the combination block, each segment $y_i[n]$ is processed to form $\tilde{y}_m[n]$ for $m = 1, 2, \ldots, d$ using phase shifts

$$\tilde{y}_m[n] = \left(\sum_{i=1}^{d} y_i[n] e^{\frac{-j2\pi(m-1)(i-1)}{d}}\right) e^{\frac{-j2\pi(m-1)n}{L}}. \tag{5}$$

For example, when $d = 4$ and $m = 1$, the combination reduces to $\tilde{y}_1[n] = y_1[n] + y_2[n] + y_3[n] + y_4[n]$.

*3) $L/d$-Point FFTs:* An $L/d$-point FFT is applied to $\tilde{y}_m[n]$ for each $m$, yielding

$$\tilde{Y}_m[k] = \sum_{n=0}^{L/d-1} \tilde{y}_m[n]\, e^{\frac{-j2\pi kn}{L/d}}, \quad k \in \{0, \ldots, L/d - 1\}. \tag{6}$$

The $L/d$-point $\tilde{Y}_m[k]$ could be seen as a downsampled version of the original $L$-point $Y[k]$ by a factor $d$, expressed as $\tilde{Y}_m[k] = Y[dk + m - 1]$. For example, when $L = 16$ and $d = 4$, the 16-point $Y[k]$ ($k = 0, \ldots, 15$) is represented by four 4-point sequences

$$\tilde{Y}_1[k] = Y[4k], \qquad \tilde{Y}_2[k] = Y[4k+1],$$
$$\tilde{Y}_3[k] = Y[4k+2], \quad \tilde{Y}_4[k] = Y[4k+3], \quad k = 0, 1, 2, 3.$$

Thus, each $\tilde{Y}_m[k]$ individually provides a downsampled view of $Y[k]$, and together the $d$ sequences contain all the information of the original spectrum without any loss.

*4) Multiplication in the Frequency Domain:* For each segment ($m = 1, 2, \ldots, d$), element-wise multiplication is performed between $\tilde{Y}_m[k]$ and the conjugate of $\tilde{C}_m[k]$, yielding

$$\tilde{R}_m[k] = \tilde{Y}_m[k]\, \tilde{C}_m^*[k]. \tag{7}$$

By substituting $\tilde{Y}_m[k]$ and $\tilde{C}_m[k]$, we find that the downsampling relationship is preserved such that $\tilde{R}_m[k] = R[dk + m - 1]$. Let $r_i[\tau] = r[\tau + (i-1)L/d]$ denote the $i$th segment of the full range profile. With this definition, the link between $\tilde{R}_m[k]$ and the segmented range profiles can be written as

$$\tilde{R}_m[k] = \sum_{\tau=0}^{L/d-1} \left(\sum_{i=1}^{d} r_i[\tau] e^{\frac{-j2\pi(dk+m-1)(i-1)}{d}}\right) e^{\frac{-j2\pi(dk+m-1)\tau}{L}}$$

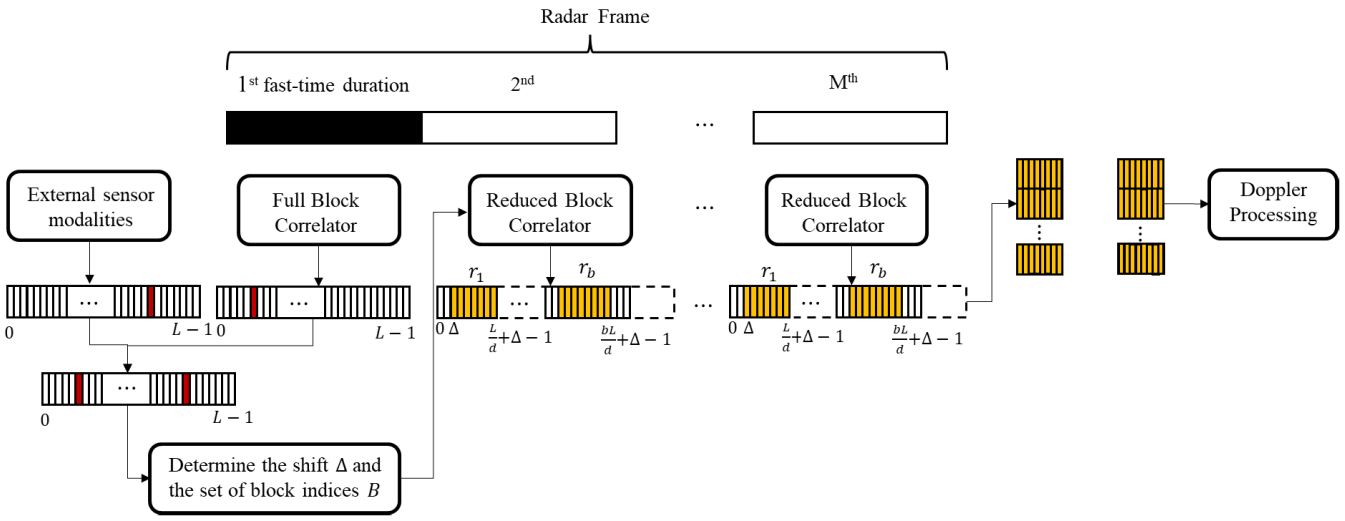


Fig. 4. Architecture of the adaptive FFT-based sliding block correlator with Doppler processing. Adaptation occurs across different frames, while each frame involves a reduced size of FFT blocks in the correlator.

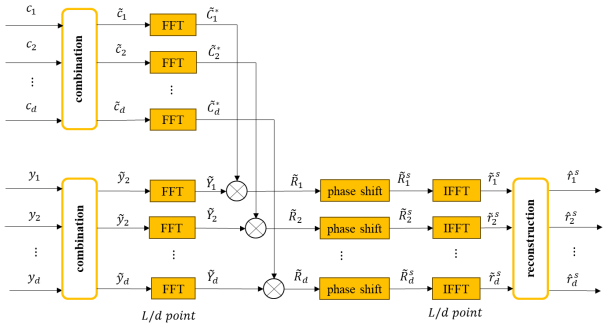


Fig. 5. Structure of sliding block FFT-based correlator.

$$= \sum_{\tau=0}^{L/d-1} \underbrace{\left( \sum_{i=1}^{d} r_i[\tau] e^{\frac{-j2\pi(m-1)(i-1)}{d}} \right) e^{\frac{-j2\pi(m-1)\tau}{L}}}_{\tilde{r}_m[\tau]} e^{\frac{-j2\pi k\tau}{L/d}}. \tag{8}$$

*5) Phase Compensation in the Frequency Domain:* To incorporate a time-domain shift of $\Delta$ samples, a corresponding linear phase shift is applied in the frequency domain. Specifically, the segment-wise frequency-domain signal $\tilde{R}_m[k]$ is modulated as follows:

$$\tilde{R}_m^s[k] = \tilde{R}_m[k] \cdot e^{-j\frac{2\pi(dk+m-1)\Delta}{L}}. \tag{9}$$

This modulation corresponds to sampling from the globally phase-compensated signal $R^s[k] = R[k] \cdot e^{-j2\pi k\Delta/L}$.

*6) L/d-Point IFFTs:* An $L/d$-point IFFT is applied to each frequency-domain segment $\tilde{R}_m^s[k]$ to obtain the corresponding time-domain sequence $\tilde{r}_m^s[\tau]$, for $\tau \in \{0, \ldots, L/d-1\}$

$$\begin{aligned}\tilde{r}_m^s[\tau] &= \frac{1}{L/d} \sum_{k=0}^{L/d-1} \tilde{R}_m^s[k] e^{\frac{j2\pi k\tau}{L/d}} \\ &= e^{\frac{-j2\pi(m-1)\Delta}{L}} \frac{1}{L/d} \sum_{k=0}^{L/d-1} \tilde{R}_m[k] e^{\frac{j2\pi k(\tau-\Delta)}{L/d}} \\ &= e^{\frac{-j2\pi(m-1)\Delta}{L}} \tilde{r}_m[\tau-\Delta]. \end{aligned} \tag{10}$$

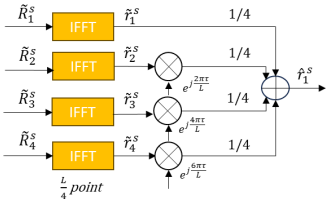


Fig. 6. Reconstruction of the first shifted range segment $\hat{r}_1^s$ for $d = 4$.

*7) Reconstruction:* Each shifted block range profile $\hat{r}_b^s$ for $b \in \{1, 2, \ldots, d\}$ could be reconstructed independently by combining the segmented components as follows:

$$\begin{aligned}\hat{r}_b^s[\tau] &= \frac{1}{d} \sum_{m=1}^{d} \tilde{r}_m^s[\tau] e^{\frac{j2\pi(m-1)\tau}{L}} e^{\frac{j2\pi(b-1)(m-1)}{d}} \\ &= \frac{1}{d} \sum_{m=1}^{d} \tilde{r}_m[\tau-\Delta] e^{\frac{j2\pi(m-1)(\tau-\Delta)}{L}} e^{\frac{j2\pi(b-1)(m-1)}{d}} \\ &= \frac{1}{d} \sum_{i=1}^{d} r_i[\tau-\Delta] \left( \sum_{m=1}^{d} e^{\frac{-j2\pi(m-1)(i-b)}{d}} \right) = r_b[\tau-\Delta]. \end{aligned} \tag{11}$$

For clarity, Fig. 6 shows the reconstruction step for the case $d = 4$, where the first shifted range segment $\hat{r}_1^s$ is recovered from the phase-shifted components $\tilde{R}_m^s$.

In practice, we are only interested in a subset of blocks defined as $B = \{b \mid b \in \mathcal{B}\}$, where $\mathcal{B} \subseteq \{1, \ldots, d\}$ is the set of block indices and $b$ denotes a block index. The cardinality $|B|$ denotes the number of selected blocks. A common optimal time shift $\Delta$ is applied uniformly across all selected blocks. This representation allows the algorithm to adaptively focus computation on the most relevant blocks while ensuring proper alignment within each selected segment.

In summary, the proposed formulation shows that the adaptive sliding block correlator can directly generate the correlation results for the desired range block without computing the full correlation profile. This selective computation

preserves the accuracy of the corresponding portion of the full-length correlator in Fig. 2, and it also reduces computational complexity as will be discussed later in Section IV-A.

### B. Stepwise Framework for Adaptive Range–Doppler Processing

Given a pre-specified block number $d$ from the radar system configuration, we now describe the stepwise framework for adaptive range–Doppler processing. The selection of $d$ is driven by the goal of reducing computational complexity, which will be illustrated in detail in Section IV-A.3. With the chosen $d$, the framework proceeds as follows.

*1) Multisource Range-Bin Selection:* To reduce computational complexity while maintaining detection performance, we adopt an adaptive range-bin selection strategy that operates on the initial radar range profile and, when available, incorporates external sensor modalities (e.g., digital maps) to guide block selection.

In our framework, the initial range profile is obtained from the first fast-time duration using the same block-based correlator with $B = \{1, \ldots, d\}$ and a fixed time shift $\Delta = 0$, ensuring that the hardware configuration remains consistent with the subsequent adaptive processing. This setting produces a range profile equivalent to that of the full-length frequency-domain correlator shown in Fig. 2, but within the block correlator structure, thereby avoiding the need to switch processing modes. Based on this initial range profile, a noise-aware thresholding algorithm—such as the constant false alarm rate (CFAR)—is then applied to identify range bins that likely contain target reflections. Similarly, digital map data can provide contextual information about road structures—such as T-junctions or bends, which helps selecting range bins that contain relevant targets based on scene topology.

By integrating radar and digital map data, it enables context-aware selection of relevant range bins, enhancing both efficiency and situational awareness. The selected bins are illustrated in red in Figs. 4 and 7.

*2) Sliding Block Selection for Efficient Processing:* Once potential targets are detected, the algorithm determines two key parameters for subsequent processing: the fractional delay $\Delta$ applied in the frequency domain to shift the block and the subset of selected blocks $B = \{b \mid b \in \mathcal{B}\}$, where $\mathcal{B} \subseteq \{1, \ldots, d\}$. The value of $\Delta$ is chosen to minimize the number of selected blocks $|B|$ while ensuring that all detected targets are fully contained within their respective blocks with sufficient margins. This sliding block mechanism enables precise target alignment while avoiding unnecessary processing of irrelevant regions. Its advantages are illustrated through two representative scenarios in Fig. 7, where a total range of $L = 1024$ bins is partitioned into $d = 4$ equal blocks of 256 bins.

*a) Case 1: single target near block boundary:* A target is located at bin 253 within the first block (bin range [0, 255]). In a nonsliding block approach, selecting block $b = 1$ risks track loss if the target crosses the boundary. Using the sliding block framework, the selection is represented as $B = \{1\}$, with $\Delta = 126$ shifting the block such that the target remains well within block 1, with sufficient margins. This adaptive alignment improves tracking robustness and highlights the advantage of the proposed sliding block strategy.

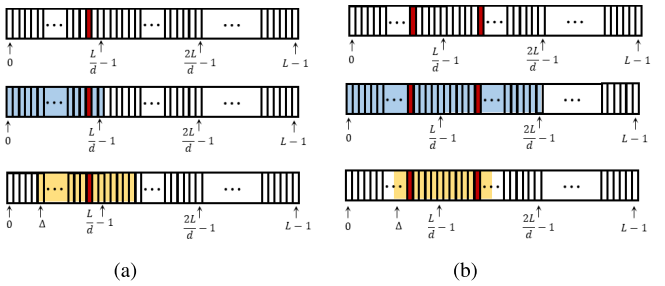


Fig. 7. Illustration of the benefits of incorporating the time-shift parameter $\Delta$ in the block selection process. Each figure shows three rows: 1) target bins (red); 2) block selection without sliding; and 3) block selection with optimal $\Delta$. (a) Case 1. (b) Case 2.

*b) Case 2: multiple nearby targets across blocks:* In a more complex scenario, two targets are detected at bins 250 and 261, which, although close in range, fall into separate blocks using the standard fixed segmentation. Without a sliding mechanism, $B = \{1, 2\}$ should be chosen, increasing computational cost. Using the sliding block framework, we estimate the average target position (approximately 255.5) and select $B = \{1\}$ with $\Delta = 127$, which shifts the block such that both targets are well-contained within block 1, with sufficient margins. This adjustment reduces the number of required blocks to a single block while maintaining detection performance, thereby significantly lowering computational complexity.

This adaptive strategy underscores the importance of jointly optimizing target localization and block configuration. The fractional delay $\Delta$ is selected to shift the block such that all detected targets are fully contained within their respective blocks with sufficient margins while minimizing the number of selected blocks $|B|$. This approach reduces computational load without compromising tracking performance. The flexibility of $\Delta$ further enables dynamic adaptation to scene changes, accommodating both target movement and clustering.

*3) Reduced FFT-Based Block Correlator:* Once the selection of sliding blocks is done, a reduced sliding block correlator is employed for the remaining $M - 1$ fast-time durations in one frame. Given $d$ blocks, optimal delay parameter $\Delta$, and the identified set $B = \{b \mid b \in \mathcal{B}\}$, the correlator reconstructs only the corresponding range profiles $\hat{r}_b^s$ by combining the segmented components $\tilde{r}_m^s$ as given in (11).

Restricting processing to the selected blocks $B$ substantially reduces computational complexity compared to full-range correlation, particularly in sparse target scenarios (see Section IV-A for a detailed complexity analysis).

*4) Frame-by-Frame Adaptation:* After each radar frame, Doppler processing is performed on the selected blocks $\hat{r}_b^s$ across all $M$ fast-time durations using $M$-point FFTs. Unlike conventional methods that require $L$ instances of $M$-point FFTs to cover the entire range, the proposed correlator processes only the blocks in $B$, which remains fixed throughout a frame. When a single sliding block is selected, the complexity is reduced to $L/d$ instances of $M$-point FFTs, significantly improving efficiency.

TABLE I
COMPLEXITY COMPARISON: FFT-BASED VERSUS ADAPTIVE BLOCK-BASED CORRELATORS

| Operation | FFT-based Correlator | Adaptive FFT-based Block Correlator | Adaptive FFT-based Sliding Block Correlator |
|---|---|---|---|
| **Range Processing** | | | |
| # MUL | $2(N_R+N_TN_R)ML\log_2 L+4N_TN_RML$ | $2(N_R+N_TN_R)ML\log_2\frac{L}{d}+4(N_T+N_T\lvert B\rvert+d+1)N_RML$ | $2(N_R+N_TN_R)ML\log_2\frac{L}{d}+4(2N_T+N_T\lvert B\rvert+d+1)N_RML$ |
| # ADD | $3(N_R+N_TN_R)ML\log_2 L+2N_TN_RML$ | $3(N_R+N_TN_R)ML\log_2\frac{L}{d}+4(1/2N_T+N_T\lvert B\rvert+d+1/2)N_RML$ | $3(N_R+N_TN_R)ML\log_2\frac{L}{d}+4(N_T+N_T\lvert B\rvert+d+1/2)N_RML$ |
| **Doppler Processing** | | | |
| # MUL | $2N_TN_RML\log_2 M$ | $2N_TN_R\lvert B\rvert M\frac{L}{d}\log_2 M$ | $2N_TN_R\lvert B\rvert M\frac{L}{d}\log_2 M$ |
| # ADD | $3N_TN_RML\log_2 M$ | $3N_TN_R\lvert B\rvert M\frac{L}{d}\log_2 M$ | $3N_TN_R\lvert B\rvert M\frac{L}{d}\log_2 M$ |

At the beginning of each new frame, the delay $\Delta$ and the set $B$ are reevaluated using the initial range profile and external sensor inputs to account for environmental or target changes. Given the short measurement interval (typically in the order of tens of ms), target displacement is minimal, and the use of the time-shift parameter $\Delta$ ensures that targets remain well-contained within their respective blocks. This frame-by-frame update maintains consistent target tracking and detection while dynamically limiting processing to the most relevant regions. As a result, the proposed method achieves substantial computational savings without compromising performance.

## IV. PERFORMANCE EVALUATION

In this section, we evaluate the performance of the proposed adaptive sliding block-based FFT correlator in comparison with the conventional full-range FFT-based correlator and our previous method [23], with emphasis on both range and Doppler processing. Section IV-A present a comparative complexity analysis of the three approaches and derive the optimal block number $d$ for efficient processing. Subsequently, simulation results are provided, including a comparison of the resulting range–Doppler maps (RDMs) and their corresponding processing times. Since Doppler processing complexity is directly impacted by the correlation stage (see Section III-B.4), it is included in the overall analysis.

### A. Complexity Analysis

Consider an MIMO configuration with $N_T \times N_R$ antennas and a slow time size $M$. The well-known computational complexity of an $N$-point FFT [24] requires $N/2\log N$ complex multiplications and $N\log N$ complex additions. Each complex multiplication consists of four real multiplications and two real additions, while a complex addition involves two real additions. We use the number of real additions and multiplications as metrics for comparing the computational costs of the baseline correlator methods with the proposed method.

*1) Complexity of Applying FFT-Based Correlator:* As shown in Fig. 2, range processing involves two $L$-point FFTs and one $L$-point IFFT. Since the FFT of the transmitted codes can be precomputed and stored, the computational complexity is determined by three main operations: computing $Y[k]$, performing multiplication in the frequency domain, and applying the IFFT. For Doppler processing in a single antenna system, we need $L$ times an $M$-point FFT. In an $N_T \times N_R$ MIMO radar configuration, the computational complexity for the range and Doppler processing steps is detailed in Table I.

*2) Complexity of the Adaptive FFT-Based Block Correlator [23]:* This method excludes the phase compensation step defined in (9); all other processing stages are retained. According to (5), the block combination step requires approximately $dL$ complex multiplications and additions, with additional $(d-1)L/d$ complex multiplications for phase alignment, which simplifies to approximately $L$. The $d$ block FFTs of length $L/d$ each require $2L\log_2(L/d)$ real multiplications and $3L\log_2(L/d)$ real additions. For the MIMO configuration, the total complexity scales with the number of transmit antennas $N_T$, the number of receive antennas $N_R$, and the number of pulses $M$. Multiplication in the frequency domain requires $N_TN_RML$ complex multiplications. The IFFT stage involves $d$ IFFTs of size $L/d$, leading to $2N_TN_RML\log_2(L/d)$ real multiplications and $3N_TN_RML\log_2(L/d)$ real additions. The final reconstruction step, based on (11), requires $(d-1)L/d$ complex operations per block. For $|B|$ relevant blocks, the total computational cost is $d(d-1)L/d$ complex multiplications and additions for the first fast-time duration and $|B|(d-1)L/d$ for each of the remaining $M-1$ durations, which can be approximated as $|B|LM$ complex multiplications and additions for simplicity. For Doppler processing, only $|B|L/d$ range bins are retained, each requiring an $M$-point FFT, reducing complexity significantly. A summary of the computational complexity is provided in Table I.

*3) Complexity of the Adaptive FFT-Based Sliding Block Correlator:* In addition to the operations in the adaptive block-based correlator, the sliding block correlator includes the phase compensation step defined in (9), which incurs an additional $N_TN_R(M-1)L$ complex multiplications. For simplicity, this is approximated as $N_TN_RML$. The resulting number of real multiplications and additions for all stages is summarized in Table I.

The total computation of the adaptive sliding block correlator can be expressed as a function of block number $d$ and the number of selected blocks $|B|$

$$\begin{aligned} f(d,|B|) &= 5\left(N_R+N_TN_R\right)ML\log_2(L/d) \\ &\quad +4\left(3N_T+2N_T|B|+2d+3/2\right)N_RML \\ &\quad +5N_TN_R|B|M\frac{L}{d}\log_2 M. \end{aligned} \tag{12}$$

As the positions of the regions of interest are unknown a priori, joint optimization of $d$ and $|B|$ is not feasible.

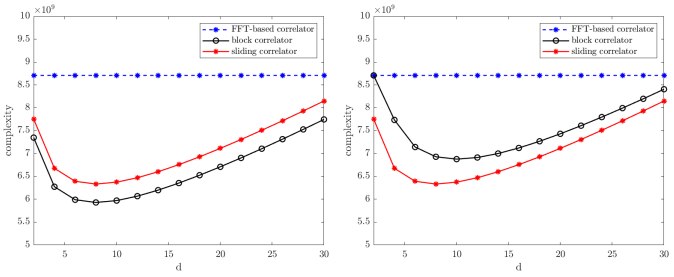


Fig. 8. Complexity comparison across different correlator configurations and block sizes $d$. (a) Single block scenario ($|B| = 1$). (b) Sliding window benefit scenario.

Instead, $d$ should be selected based on radar configuration and kept fixed, while $|B|$ adapts dynamically to the determined target distribution. To determine the optimal block number $d^*$, we consider the idealized case where all detected targets fall within a single block (i.e., $|B| = 1$) and minimize $f(d, 1)$ with respect to $d$. Differentiating $f(d, 1)$ and setting the derivative to zero yields a quadratic equation in $d$, whose larger root provides the practical solution. Thus, the optimal block number is given by

$$d^* = \frac{5N_T + 5}{16 \ln 2} + \frac{\sqrt{(5N_T + 5)^2 + 160N_T \ln 2 \log_2 M}}{16 \ln 2}. \quad (13)$$

In practice, $d^*$ is rounded to the nearest integer that divides the total number of range bins $L$, ensuring valid FFT segmentation.

*4) Complexity Comparison:* We now assess the computational complexity of the fixed and adaptive correlators in terms of operations shown in Table I. For evaluation, we consider a $4 \times 4$ MIMO configuration and slow time size of $M = 2048$. The complexity is analyzed using a Gold sequence of length 2047. Since FFT operations require zero padding to the nearest power of two, we set $L = 2048$. Under this configuration and the assumption of a single relevant block ($|B| = 1$), the optimal block number $d^*$ is analytically determined to be approximately 8.

Fig. 8(a) presents the complexity trends when both the block-based and sliding block correlators operate with $|B| = 1$. Both adaptive methods significantly reduce computational cost compared to the conventional full-range frequency-domain correlator across different block sizes $d$. The lowest complexity for both occurs at $d = 8$, aligning with the analytically derived optimal $d^*$. At this point, the block-based correlator achieves approximately a 32% reduction in complexity, while the sliding block correlator achieves a 27% reduction due to the additional cost of frequency-domain phase compensation. Although slightly higher, this remains more efficient than the full-range method.

Fig. 8(b) demonstrates the advantage of the sliding window in scenarios like Case 2 [illustrated in Fig. 7(b)], where it enables a reduction in the number of required blocks: $|B| = 2$ for the block correlator and $|B| = 1$ for the sliding block correlator. The results show that the sliding block correlator now outperforms the block correlator in total complexity due to fewer reconstructed blocks.

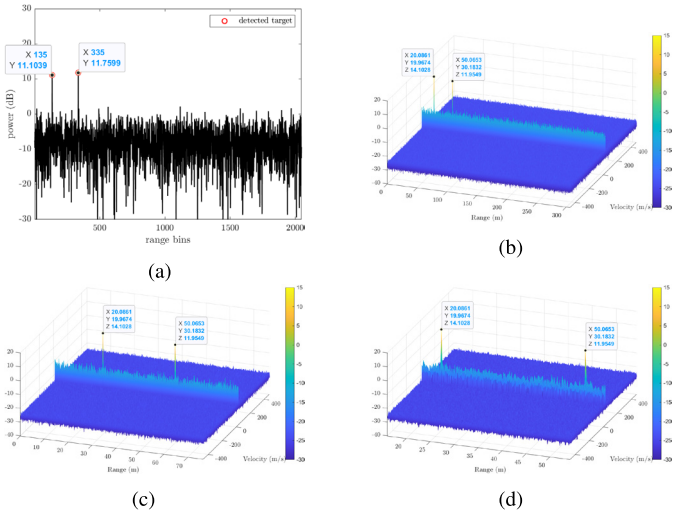


Fig. 9. Initial range profile and RDMs for Scenario 1. (a) Initial range profile. (b) RDM with full FFT-based correlator. (c) RDM with adaptive FFT-based block correlator. (d) RDM with adaptive FFT-based sliding block correlator.

## B. Simulation Results

We retain the same configuration as in the complexity analysis: a $4 \times 4$ MIMO radar with a slow time size of $M = 2048$, using a Gold sequence of length 2047. All simulations include additive thermal noise with a power spectral density of $-177$ dBm/Hz and are conducted with a block number of $d = 8$.

*1) Scenario 1: Two-Target Case:* In this scenario, two targets are considered: a car with radar cross section (RCS) of 10 dBsm located at 20 m and 10°, moving at 20 m/s; and a truck with an RCS of 25 dBsm located at 50 m and $-5°$, moving at 30 m/s. From the initial range profile [Fig. 9(a)], the relevant range bins are identified at 135 and 335.

Using a fixed-block correlator, these targets fall into two separate blocks, $B = \{1, 2\}$, as shown in Fig. 9(c). In contrast, the adaptive sliding block correlator leverages target clustering and selects $B = \{1\}$ with $\Delta = 107$, shifting block 1 that both detections are fully contained within a single block with sufficient margins. The resulting RDM is presented in Fig. 9(d).

Fig. 9 shows that both adaptive correlators preserve the target peaks and maintain the same noise floor, resulting in comparable signal-to-noise ratio (SNR) and detection performance. In terms of runtime, the full FFT-based correlator requires 14.29 s, whereas the adaptive block correlator with $|B| = 2$ reduces this to 8.22 s. The sliding block correlator, though slightly more costly due to frequency-domain phase compensation, achieves a runtime of 6.79 s by reducing the block count to $|B| = 1$, outperforming the adaptive block approach. These results align with the complexity trends in Fig. 8(b), where the additional cost of phase compensation is outweighed by the computational savings from processing fewer blocks. Although these simulations are performed in MATLAB and do not reflect hardware execution, the reductions in processing time are indicative of potential efficiency gains achievable in real-time embedded implementations.

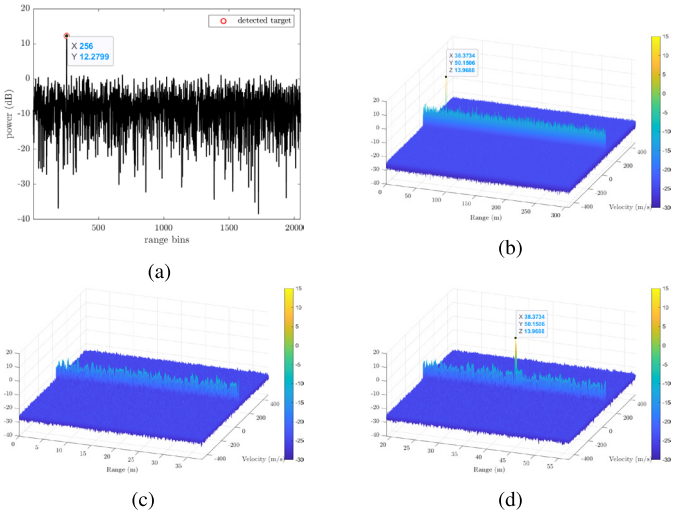


Fig. 10. Initial range profile and RDMs for Scenario 2. (a) Initial range profile. (b) RDM with full FFT-based correlator. (c) RDM with adaptive FFT-based block correlator. (d) RDM with adaptive FFT-based sliding block correlator.

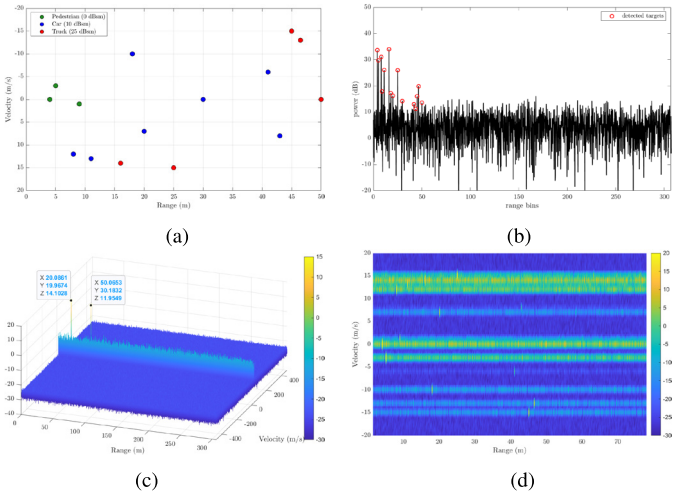


Fig. 11. Dense multitarget scenario. (a) Target distribution. (b) Initial range profile. (c) RDM with full FFT-based correlator. (d) RDM with adaptive FFT-based sliding block correlator.

*2) Scenario 2: Single Target Near Block Edge:* In this scenario, a single target is considered: an object with an RCS of 20 dBsm located at 38.22 m and 0°, a relative velocity of 50 m/s. From the initial range profile [Fig. 10(a)], the detected target appears at range bin 256, which lies at the boundary of block 1. Using a fixed-block correlator, the selection is $B = \{1\}$, and the corresponding RDM is shown in Fig. 10(c). However, due to the target's motion during the frame, the target peak does not appear in the RDM, leading to potential track loss. In contrast, the adaptive sliding block correlator selects $B = \{1\}$ with a $\Delta = 127$, shifting the block to ensure the target remains within the processed region. The resulting RDM, shown in Fig. 10(d), successfully captures the target.

Fig. 10 shows that both adaptive correlators preserve target peaks and noise levels, ensuring similar SNR and detection. In terms of runtime, the full correlator requires 15.532 s, whereas the adaptive block correlator reduces this to 6.00 s. The sliding block correlator, though slightly more costly due to frequency-domain phase compensation, achieves a runtime of 6.53 s, still significantly faster than the full correlator. These results are consistent with the complexity trends in Fig. 8(a), where the additional cost of phase compensation offsets some of the gains when $|B|$ is identical across methods.

*3) Scenario 3: Dense Multiple Targets:* In this scenario, a dense environment is considered with multiple objects of different types distributed across the range–Doppler plane. This scenario represents a complex traffic setting with closely spaced targets and a mix of RCS values. Fig. 11(a) illustrates the distribution of these targets in range and velocity, with their RCS values shown in different colors.

From the initial range profile [Fig. 11(b)], target candidates are within blocks $B = \{1, 2\}$. We reconstruct these blocks with a common shift $\Delta = 10$ to maintain margins. The resulting runtime is 8.14 s, which remains substantially lower than that of the full FFT correlator (13.54 s). A comparison between the adaptive sliding RDMs [Fig. 11(d)] and the full-FFT RDM [Fig. 11(c)] confirms that target peaks and the noise floor are preserved, thereby maintaining detection performance.

In summary, the first two scenarios demonstrate the benefits of sliding by consolidating two fixed blocks into a single processed block—thereby eliminating redundant computation, and by preventing track loss for fast targets near block boundaries. The third scenario showcases the robustness of the proposed method in dense, multitarget driving scenarios.

## V. Conclusion

This work proposed a sliding block-based FFT correlator for PMCW radar systems, aimed at reducing computational complexity while maintaining detection performance. Building on our prior work [23], the proposed method introduces a time-shift parameter $\Delta$ to adaptively align processing blocks with target positions, reducing boundary effects and the number of blocks required. Range-bin selection may be done by integrating external sensor inputs or by using an initial range profile of one pulse. Finally, we derive the optimal block size $d^*$ through analytical complexity minimization. Simulation results confirm that the proposed method preserves SNR and improves runtime efficiency compared to both conventional and fixed-block-based adaptive correlators. In a future step, the proposed complexity gains should be validated on FPGAs/ASICs for real-time automotive PMCW radar processing as done in [25] and [26].

Future work could explore integrating the proposed correlation methods with mismatched filters. Mismatched filters, which are designed to reduce the integrated sidelobe level and increase the peak-to-sidelobe ratio, offer an alternative approach to enhancing detection performance in challenging target environments [27], [28], [29]. By incorporating mismatched filter designs into the proposed adaptive block-based framework, effective means of mitigating sidelobe and improving dynamic range at low complexity can become possible.

Another future direction is the application of the proposed method to the few/mixed-bit ADC PMCW systems considered in [30] and [31].

## REFERENCES


[1] F. Engels, P. Heidenreich, M. Wintermantel, L. Stäcker, M. Al Kadi, and A. M. Zoubir, "Automotive radar signal processing: Research directions and practical challenges," *IEEE J. Sel. Topics Signal Process.*, vol. 15, no. 4, pp. 865–878, Jun. 2021.

[2] F. Roos, J. Bechter, C. Knill, B. Schweizer, and C. Waldschmidt, "Radar sensors for autonomous driving: Modulation schemes and interference mitigation," *IEEE Microw. Mag.*, vol. 20, no. 9, pp. 58–72, Sep. 2019.

[3] S. Sun, A. P. Petropulu, and H. V. Poor, "MIMO radar for advanced driver-assistance systems and autonomous driving: Advantages and challenges," *IEEE Signal Process. Mag.*, vol. 37, no. 4, pp. 98–117, Jul. 2020.

[4] D. Schwarz, N. Riese, I. Dorsch, and C. Waldschmidt, "System performance of a 79 GHz high-resolution 4D imaging MIMO radar with 1728 virtual channels," *IEEE J. Microw.*, vol. 2, no. 4, pp. 637–647, Oct. 2022.

[5] B. Schweizer et al., "The fairy tale of simple all-digital radars: How to deal with 100 Gbit/s of a digital millimeter-wave MIMO radar on an FPGA [application notes]," *IEEE Microw. Mag.*, vol. 22, no. 7, pp. 66–76, Jul. 2021.

[6] N. Karimian-Sichani, M. Alaee-Kerahroodi, B. S. M. R. Rao, E. Mehrshahi, and S. A. Ghorashi, "Antenna array and waveform design for 4-D-imaging mmWave MIMO radar sensors," *IEEE Trans. Aerosp. Electron. Syst.*, vol. 60, no. 2, pp. 1848–1864, Apr. 2024.

[7] D. Guermandi et al., "A 79-GHz 2 × 2 MIMO PMCW radar SoC in 28-nm CMOS," *IEEE J. Solid-State Circuits*, vol. 52, no. 10, pp. 2613–2626, Oct. 2017.

[8] M. Kahlert, T. Fei, C. Tebruegge, and M. Gardill, "Stepped-frequency PMCW waveforms for automotive radar applications," *IEEE Trans. Radar Syst.*, vol. 3, pp. 233–245, 2025.

[9] V. Oliari, W. van Houtum, and A. Pandharipande, "Reconfigurable PMCW radar sensor system," *IEEE Sensors Lett.*, vol. 7, no. 11, pp. 1–4, Nov. 2023.

[10] R. Amar, M. Alaee-Kerahroodi, and M. R. B. Shankar, "Polynomial phase constrained waveforms for mmWave MIMO radars," *IEEE Trans. Aerosp. Electron. Syst.*, vol. 61, no. 4, pp. 8225–8243, Aug. 2025.

[11] S. Alland, W. Stark, M. Ali, and M. Hegde, "Interference in automotive radar systems: Characteristics, mitigation techniques, and current and future research," *IEEE Signal Process. Mag.*, vol. 36, no. 5, pp. 45–59, Sep. 2019.

[12] S. W. Golomb and G. Gong, *Signal Design for Good Correlation: For Wireless Communication, Cryptography, and Radar*. Cambridge, U.K.: Cambridge Univ. Press, 2005.

[13] H. He, J. Li, and P. Stoica, *Waveform Design for Active Sensing Systems: A Computational Approach*. Cambridge, U.K.: Cambridge Univ. Press, 2012.

[14] W. Van Thillo, P. Gioffré, V. Giannini, D. Guermandi, S. Brebels, and A. Bourdoux, "Almost perfect auto-correlation sequences for binary phase-modulated continuous wave radar," in *Proc. Eur. Microw. Conf.*, Oct. 2013, pp. 1803–1806.

[15] T. Maeda, S. Kanemoto, and T. Hayashi, "A novel class of binary zero-correlation zone sequence sets," in *Proc. IEEE Region 10 Conf. (TENCON)*, Nov. 2010, pp. 708–711.

[16] A. M. D. Turkmani and U. S. Goni, "Performance evaluation of maximal-length, gold and Kasami codes as spreading sequences in CDMA systems," in *Proc. 2nd IEEE Int. Conf. Universal Pers. Commun.*, Oct. 1993, pp. 970–974.

[17] P. K. Enge, "The global positioning system: Signals, measurements, and performance," *Int. J. Wireless Inf. Netw.*, vol. 1, no. 2, pp. 83–105, Apr. 1994.

[18] D. Akopian and S. Agaian, "A fast time-recursive correlator for DSSS communications," *IEEE Signal Process. Lett.*, vol. 15, pp. 589–592, 2008.

[19] D. Akopian and S. Agaian, "Fast and parallel matched filters in time domain," in *Proc. 17th Int. Tech. Meeting Satell. Division Inst. Navigat. (ION GNSS)*, 2004, pp. 491–500.

[20] D. Akopian, P. Sagiraju, and B. Nowak, "Fast time-recursive block correlators for pseudorandom sequences," *IEEE Trans. Circuits Syst. I, Reg. Papers*, vol. 60, no. 7, pp. 1835–1844, Jul. 2013.

[21] J. Leclère, C. Botteron, R. J. Landry, and P.-A. Farine, "FFT splitting for improved FPGA-based acquisition of GNSS signals," *Int. J. Navigat. Observ.*, vol. 2015, pp. 1–12, Dec. 2015.

[22] J. Leclére, "Resource-efficient parallel acquisition architectures for modernized GNSS signals," Tech. Rep. EPFL Thesis 6190, 2014.

[23] H. Wu, G. Leus, and A. Pandharipande, "Adaptive frequency-domain block correlators for range processing in digital automotive radars," in *Proc. 33rd Eur. Signal Process. Conf. (EUSIPCO)*, 2025, pp. 2212–2216.

[24] R. G. Lyons, *Understanding Digital Signal Processing*, 3rd ed., Upper Saddle River, NJ, USA: Prentice-Hall, 2010.

[25] M. Caffa, F. Biletta, and R. Maggiora, "Binary-phase vs. Frequency modulated radar measured performances for automotive applications," *Sensors*, vol. 23, no. 11, p. 5271, Jun. 2023.

[26] J. Zhao, Q. Liu, and B. Tan, "Design of PMCW millimeter-wave radar algorithms on an embedded DSP," in *Proc. 16th Int. Conf. Signal Process. Syst. (ICSPS)*, Mar. 2025, p. 165.

[27] Y. Chen, R. Lin, Y. Cheng, and J. Li, "Joint design of periodic binary probing sequences and receive filters for PMCW radar," *IEEE Trans. Signal Process.*, vol. 70, pp. 5996–6010, 2022.

[28] A. Sakhnini, M. Bauduin, A. Bourdoux, and S. Pollin, "Mismatched filters for high-velocity target detection in PMCW radars," in *Proc. 20th Eur. Radar Conf. (EuRAD)*, Sep. 2023, pp. 114–117.

[29] C. Onen, H. Wu, and A. Pandharipande, "Block-based mismatched filters for self-interference mitigation in PMCW radars," in *Proc. 33rd Eur. Signal Process. Conf. (EUSIPCO)*, 2025, pp. 2222–2226.

[30] C.-Y. Wu, J. Ren, T. F. Wong, and J. Li, "Computationally efficient implementation of SLIM for parameter estimation in few-bit PMCW MIMO radar systems," *IEEE Trans. Radar Syst.*, vol. 1, pp. 339–352, 2023.

[31] X. Shang, R. Lin, and Y. Cheng, "Mixed-ADC based PMCW MIMO radar angle-Doppler imaging," *IEEE Trans. Signal Process.*, vol. 72, pp. 883–895, 2024.